

Differentiable Physics-Driven Human Representation for Millimeter-Wave Based Pose Estimation

Shuntian Zheng¹, Guangming Wang², Jiaqi Li¹, Minzhe Ni¹, Yu Guan¹

¹University of Warwick, United Kingdom

²University of Cambridge, United Kingdom

shuntian.zheng@warwick.ac.uk, gw462@cam.ac.uk, jiaqi.li.16@warwick.ac.uk, minzhe.ni@warwick.ac.uk, yu.guan@warwick.ac.uk

Abstract

While millimeter-wave (mmWave) presents advantages for Human Pose Estimation (HPE) through its non-intrusive sensing capabilities, current mmWave-based HPE methods face limitations in two predominant input paradigms: Heatmap and Point Cloud (PC). Heatmap represents dense multi-dimensional features derived from mmWave, but is significantly affected by multipath propagation and hardware modulation noise. PC, a set of 3D points, is obtained by applying the Constant False Alarm Rate algorithm to the Heatmap, which suppresses noise but results in sparse human-related features. To address these limitations, we study the feasibility of providing an alternative input paradigm: Differentiable Physics-driven Human Representation (DIPR), which represents humans as an ensemble of Gaussian distributions with kinematic and electromagnetic parameters. Inspired by Gaussian Splatting, DIPR leverages human kinematic priors and mmWave propagation physics to enhance human features while mitigating non-human noise through two strategies: 1) We incorporate prior kinematic knowledge to initialize DIPR based on the Heatmap and establish multi-faceted optimization objectives, ensuring biomechanical validity and enhancing motion features. 2) We simulate complete mmWave processing pipelines, re-render a new Heatmap from DIPR, and compare it with the original Heatmap, avoiding spurious noise generation due to kinematic constraints overfitting. Experimental results on three datasets with four methods demonstrate that existing mmWave-based HPE methods can easily integrate DIPR and achieve superior performance.

1 Introduction

Millimeter-wave (mmWave) has emerged as a promising modality for Human Pose Estimation (HPE) due to its advantages in privacy preservation and robustness to ambient lighting conditions (Zhao et al. 2018a,b). Unlike optical sensors or wearable devices, mmWave radar can directly capture the target’s distance, angular position, and radial velocity through electromagnetic wave modulations, offering unique capabilities for HPE (Sengupta and Cao 2022; Chang et al. 2020). Furthermore, the large bandwidth of mmWave enables superior spatial resolution compared to other wireless signals such as Wi-Fi, making it particularly suitable for precise indoor human sensing (Zhang et al. 2024).

Current mmWave-based HPE methods primarily utilize two input paradigms: Heatmap and Point Cloud (PC) (Cao

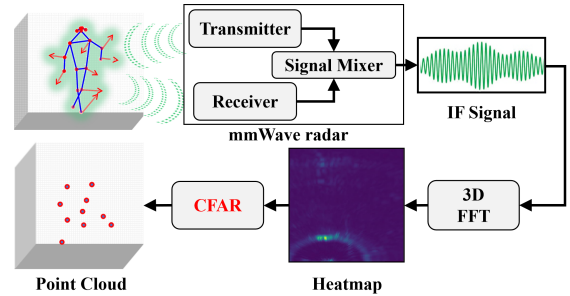


Figure 1: mmWave processing flow.

et al. 2022; Sengupta et al. 2020; Rahman et al. 2024). Heatmap is a multi-dimensional data structure generated through Frequency-Modulated Continuous-Wave (FMCW) signal processing and Fourier transform of raw mmWave, while PC is subsequently derived by applying the Constant False Alarm Rate (CFAR) algorithm (Rohling 1983) to extract sparse peak coordinates from the Heatmap (Fig. 1).

However, both paradigms face limitations: Heatmap contains dense information, but suffers from complex noise arising from mmWave multipath propagation on non-human objects and hardware-induced artifacts (Gurbuz and Amin 2019; Jayaweera et al. 2024). While PC contains less noise, it suffers from sparsity issues after threshold-based peak detection in the CFAR algorithm, hindering the capture of fine-grained human motion (An, Li, and Ogras 2022).

Recent research has attempted to address this information-noise trade-off through various approaches. Some methods (Zhang, Geng, and Lin 2021; Yataka et al. 2024; Fan et al. 2024) employ pre-trained deep learning modules for feature extraction and denoising, yet lack theoretical guarantees for optimal human pose feature separation from noise. Alternative approach (Ding et al. 2024) introduces additional training information, but its feature distributions deviate from authentic mmWave.

Drawing inspiration from Gaussian Splatting (Wu et al. 2024), which employs Gaussian distributions to store and optimize the objects’ optical properties, we introduce “Differentiable Physics-driven Human Representation” (DIPR), a tailored feature template especially for mmWave-based HPE (Fig. 2) as an alternative input paradigm, to ad-

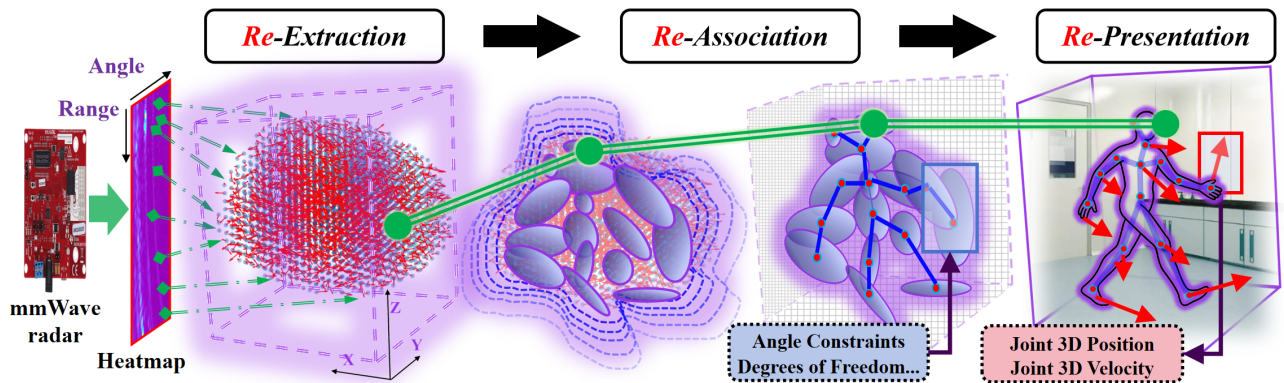


Figure 2: The preparation pipeline of Differentiable Physics-driven Human Representation (DIPR), which includes: 1) Extracting primitive motion features; 2) Associating features through optimization; 3) Presenting human action states with the DIPR.

address the aforementioned limitations of Heatmap and PC. DIPR can be generated via a process named “MmWave Gaussian Splatting” (M-GS), with three key components comprising: 1) Re-Extraction: Extract spatial activity and velocity-induced phase distributions from Heatmap to initialize Gaussian parameters and establish biomechanical constraints. 2) Re-Association: Initialize Gaussian distributions for all joints, and guide collaborative gradient descent of parameters through kinematic constraints and consistency with original signal patterns. 3) Re-Presentation: Consolidate optimized Gaussian parameters into DIPR.

The contributions are as follows:

- We study the feasibility of providing an alternative input paradigm for mmWave-based HPE by proposing Differentiable Physics-driven Human Representation (DIPR) and its synthesis method, MmWave Gaussian Splatting (M-GS). DIPR models the human as a Gaussian ensemble encoded with kinematic and electromagnetic parameters, serving as a universal input paradigm that can be easily integrated into existing HPE approaches. To the best of our knowledge, this constitutes the first adaptation of Gaussian Splatting to the mmWave-based HPE and proposes a new input paradigm for it.
- We design two modules in M-GS that extract spatial activity features and spatial velocity features, initialize and optimize specialized Gaussian distributions through modular constraints that enforce biomechanical plausibility. Meanwhile, to avoid spurious motion generation from overfitting, we develop a radar processing module in M-GS, converting DIPR’s parameters back to the Heatmap for signal consistency validation (Fig. 3).
- We conduct comprehensive experiments on three datasets with four state-of-the-art HPE methods, demonstrating DIPR’s effectiveness, along with its adaptability and performance boost abilities with existing methods.

2 Related work

2.1 HPE Based on mmWave

Current mmWave-based HPE methods primarily utilize two input paradigms: Heatmap and Point Cloud (PC). Heatmap

preserves dense human motion features, but has seen limited adoption due to the noise artifacts. Recent efforts have been made to address this issue. RETR (Yataka et al. 2024) explores multi-view fusion for noise suppression, albeit at increased complexity caused by the pre-trained module. ProbRadarM3F (Zhu et al. 2024) advances by incorporating probabilistic spatial mapping, yet focuses exclusively on overall spatial patterns while neglecting the unique patterns of human. While some studies (Nibali et al. 2019; Xue et al. 2023) attempt to extract human-related temporal features from Heatmap, their reliance on deep learning modules overlooks mmWave propagation and reflection principles.

PC, derived from Heatmap through Constant False Alarm Rate (CFAR) algorithm (Fig. 4) (Rohling 1983), offers enhanced signal-to-noise ratio. Early approaches (An and Ogras 2022; Sengupta et al. 2020; Singh et al. 2019) favor PC for its deep learning compatibility, despite its inherent sparsity. FUSE (An and Ogras 2022) introduces a pose tracking framework but exhibits limitations in capturing rapid joint movements. A recursive method is proposed (Bi et al. 2023) to enhance PC through spatial-temporal clustering, yet it demonstrates vulnerability in limb overlap scenarios. Recent approaches leverage inter-frame correlations for explicit temporal features to boost accuracy. For instance, mmDiff (Fan et al. 2024) employs a diffusion-based (Ho, Jain, and Abbeel 2020) refinement module for pose estimation. However, in order to obtain the optimization guidance that contains human features while minimizing noise for the diffusion module, mmDiff had to employ pre-trained ResNet (He et al. 2016) modules for preprocessing, resulting in high computational overhead.

There have emerged works to enhance existing input paradigms: A deep learning-based PC enhancement method is proposed (Zhang, Geng, and Lin 2021), though it heavily relies on extensive labeled datasets. Scene flow estimation is introduced (Ding et al. 2024) to augment the information density of PC but struggles with accurate spatial feature alignment across modalities. A simulation method is employed (Wang et al. 2023) to generate additional supervisory information, but combinations of mathematical transformations cannot fully capture real-world signal complexities.

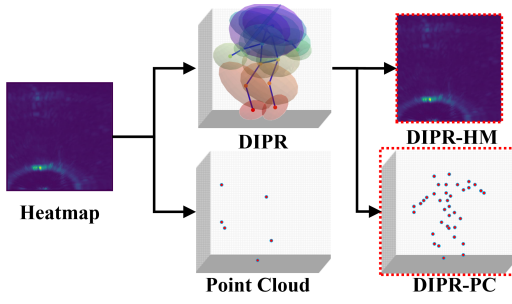


Figure 3: Reverse projection of DIPR into conventional paradigms: DIPR-HeatMap (DIPR-HM) and DIPR-PC.

2.2 Optical Signal Representations

Advances in the field of computer vision offer valuable insights. Gaussian-based representations have emerged as particularly relevant approaches. Gaussian Splatting (GS) (Wu et al. 2024) demonstrates the effectiveness of parameterized Gaussian distributions in modeling 3D scenes through geometric and optical attributes, enabling real-time, high-fidelity rendering. GS has been extended to dynamic scenes (Luiten et al. 2024), where the temporal evolution captures object motion.

Recent works have introduced Gaussian distribution-based modeling for humans. HUGS (Kocabas et al. 2024) employs 3D Gaussians to refine SMPL-based (Loper et al. 2023) human models, achieving rendering acceleration through decoupled background-human rendering. 3D Gaussians have been applied to optimize dynamic human features, including fine-grained clothing texture rendering (Li et al. 2024) and motion generation (Abdal et al. 2024).

These developments highlight the Gaussian distribution’s potential as a representation element, offering storage, optimization, and expressive capabilities. Such characteristics suggest promising applications in mmWave-based HPE.

However, direct adaptation of GS faces challenges: 1) The mmWave signal exhibits distinct physical properties, including multipath propagation, material penetration, and complex reflection patterns (Niu et al. 2015), necessitating specialized parameterization; 2) The lower resolution of mmWave radars (Rahman et al. 2024), compared to optical sensors, demands either enhanced feature extraction or the incorporation of prior knowledge for high-quality HPE.

3 Problem Statement

HPE based on mmWave confronts “information-noise trade-off” challenges, specifically:

1) Existing approaches are constrained to only two input paradigms that exhibit limited correlation with human kinematic characteristics. Heatmap constitutes the output of the radar processing (Fig.1), wherein noise introduced by environmental objects and radar hardware artifacts cannot be effectively eliminated. While it retains abundant human-related information, the continuous kinematic features become obscured by noise contamination. PC, although achieving signal-to-noise ratio enhancement through

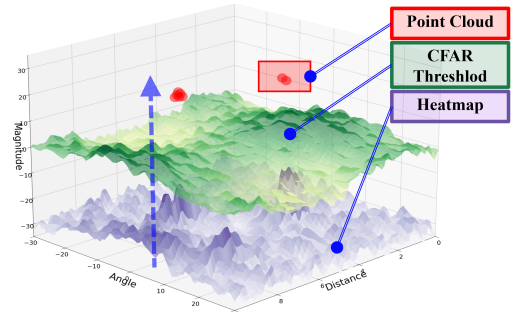


Figure 4: Denoising by Constant False Alarm Rate (CFAR).

CFAR algorithm based on Heatmap, suffers from sparsity in the signal density and human features quantity.

2) Existing enhancement approaches neglect leveraging human-specific kinematic priors and lack data structures capable of explicitly representing and optimizing parameters inherent to human motion in mmWave. For example, mPoint (Zhang, Geng, and Lin 2021) employs trainable or pre-trained neural network modules for enhancement, which introduces a black-box property and cannot fully guarantee post-training fidelity in modeling kinematic characteristics, while imposing substantial computational overhead. Other methods (Ding et al. 2024; Wang et al. 2023) integrate cross-modal knowledge or construct additional supervision. However, these approaches suffer from modeling discrepancies across different modalities and require manual curation of diverse supervisory sources, which cannot comprehensively simulate authentic human features or non-human noise. Meanwhile, vision-based Gaussian distribution modeling (Wu et al. 2024) has shown potential. By integrating kinematic features into Gaussian parameters, we establish robust correlations between parameters and mmWave based on signal perturbation patterns (Chen et al. 2006) for optimization, while maintaining low complexity as shown in the Supplementary.

4 Preliminaries

4.1 mmWave Radar Processing

The mmWave radar transmits signals with linear frequency modulation (Fig. 1), the output Heatmap contains range, velocity, and angle dimensions through three key processing steps (Iovescu and Rao 2020). 1) Range processing extracts distance through the time delay between transmitted and received chirps, which creates a frequency difference proportional to range and is detected via the Fast Fourier Transform (FFT) on the Intermediate Frequency (IF) signal (Fig.1). 2) Velocity processing captures motion through Doppler frequency shifts (Chen et al. 2006) $\Delta f = 2v_r/\lambda$, where v_r is radial velocity and λ is radar wavelength, detected through the second FFT across chirp periods. 3) Angle processing enables spatial 3D localization through phase differences between antenna elements, where azimuth angle θ_{az} and elevation angle θ_{el} are computed as $\theta_{az} = \sin^{-1}(\lambda\Delta\Phi_{az}/2\pi l_{az})$ and $\theta_{el} = \sin^{-1}(\lambda\Delta\Phi_{el}/2\pi l_{el})$ respectively, with l_{az} and l_{el} representing antenna spacing in horizontal and vertical

arrays, and $\Delta\Phi_{az}$ and $\Delta\Phi_{el}$ denoting the measured phase differences, extracted through the third FFT across antenna elements. Meanwhile, unlike optical signals, radar signals travel from the transmitter to the target and back (Piersanti, Annoni, and Cassioli 2012), resulting in $1/r^4$ power attenuation where r is the range distance.

The subsequent processing involves Constant False Alarm Rate algorithm (Rohling 1983) (Fig. 4), which employs an adaptive threshold to suppress clutter in the Heatmap.

4.2 Gaussian Splatting (GS)

Gaussian Splatting has emerged as a new approach in computer vision for representing 3D scenes through collections of parameterized Gaussian primitives, enabling real-time, high-fidelity rendering. The foundation of GS (Wu et al. 2024) relies on four key mathematical formulations.

- (1) Each Gaussian is parameterized by a distribution:

$$G(x) = \exp\left(-\frac{1}{2}(x-p)^T \Sigma^{-1}(x-p)\right), \quad (1)$$

where $p \in \mathbb{R}^3$ represents the centroid position and $\Sigma \in \mathbb{R}^{3 \times 3}$ defines the covariance matrix encoding the Gaussian's shape and orientation in 3D space.

- (2) The covariance matrix is decomposed into rotation and scaling components for stable optimization:

$$\Sigma = RSS^T R^T, \quad (2)$$

where R is the rotation matrix derived from unit quaternions, and $S = \text{diag}(s_x, s_y, s_z)$ contains the scaling factors along principal axes. This decomposition ensures positive semi-definiteness and numerical stability during optimization.

- (3) Alpha blending to composite overlapping Gaussians:

$$C = \sum_{i=1}^N c_i \alpha_i \prod_{j=1}^{i-1} (1 - \alpha_j), \quad (3)$$

where c_i and α_i represent the color and opacity of the i -th Gaussian ordered by depth, ensuring proper occlusion handling and smooth appearance transitions.

- (4) The rendering process projects 3D Gaussians onto the image plane through differentiable rasterization:

$$C(u) = \sum_{i=1}^N c_i \alpha_i \prod_{j=1}^{i-1} (1 - \alpha_j) \cdot \exp\left(-\frac{(u-u_i)^T \Sigma_i^{-1} (u-u_i)}{2}\right), \quad (4)$$

where $C(u)$ is the color at pixel u , u_i is the projected position of the i -th Gaussian on the image plane.

5 Methodology

In this section, we introduce mmWave Gaussian Splatting (M-GS), based on which Differentiable Physics-driven Human Representation (DIPR) can be generated for mmWave-based HPE. The M-GS includes four modules: 1) Position and velocity extract module; 2) Parameter initialization (Fig. 5 (A)); 3) Re-render module (Fig. 5 (C)); 4) Optimization.

5.1 Extracting Position and Velocity

The first step is extracting position and velocity state from the three-dimensional radar Heatmap $H \in \mathbb{R}^{R \times V \times A}$, where R , V , and A represent range, Doppler velocity, and angle. This process converts the radar's raw intensity measurements into spatial coordinates and motion vectors that can be used to initialize human kinematic parameters.

Unlike the CFAR, which extracts discrete points by thresholding across all dimensions (Rohling 1983), the M-GS maintains relative intensity relationships across range-velocity-angle combinations in the Heatmap H . This mapping preserves the continuous intensity distribution without applying hard thresholds, ensuring that weak but kinematically consistent signals are retained. The H coordinates are then transformed to Cartesian space using the geometric relationships: range r provides radial distance, and angle θ determines the angle of arrival. The transformation follows $x = r \cos(\theta)$, $y = r \sin(\theta)$, $z = \sqrt{r^2 - x^2 - y^2}$. This yields coarse positions $X_{coarse} = [x, y, z]$.

The velocity state V_{coarse} can also be extracted from H . First, the velocity v_d is from the V dimension at the detected position based on the Doppler principle (Iovescu and Rao 2020). Then, the radial velocity v_r is computed as $v_r = v_d \cdot \cos(\theta_{az}) \cdot \cos(\theta_{el})$ where θ_{az} and θ_{el} are the azimuth and elevation angles respectively. Finally, the velocity is reconstructed using the relationships: $v_x = v_r \cdot \cos(\theta_{az})$, $v_y = v_r \cdot \sin(\theta_{az})$, and $v_z = v_r \cdot \sin(\theta_{el})$.

Using these modules, we can extract $X_{coarse} = [x, y, z]$ and $V_{coarse} = [v_x, v_y, v_z]$ from H , containing coarse spatial position features and velocity state features, respectively.

5.2 Joint Association and Presentation

Based on X_{coarse} and V_{coarse} , we can represent and optimize the human as an ensemble of Gaussian primitives with radar-specific kinematic parameters, filter out non-human noise while preserving human features.

Drawing from GS's design (Eq. 1), we model the human body as a collection of N Gaussian primitives $\{\Theta_i\}_{i=1}^N$, where each joint i is characterized by a set of six parameters to capture both spatial and kinematic properties (Fig. 5) (B):

$$\Theta_i = \{p_i, s_i, q_i, v_i, \beta_i, \phi_i\}, \quad (5)$$

The six parameters are described as follows.

Four parameters inherit designs from prior work: (1) Position $p_i \in \mathbb{R}^3$, which represents the spatial centroid of joint i in 3D coordinates, initialized using T-pose (Bao, Zhao, and Qian 2024). (2) Scale $s_i \in \mathbb{R}^3$ which defines anisotropic scaling factors along principal axes, encoding the anatomical extent of joint influence regions, and (3) Opacity $\beta_i \in \mathbb{R}$ which modulates radar reflection intensity and contribution strength. These three parameters adopt the modeling methodology for light signal perturbation on objects as referenced in GS (Eq. 1, 2). (4) Rotation $q_i \in \mathbb{R}^4$, a unit quaternion parameterizing 3D orientation ensuring smooth rotational transitions, derives from the 6D human motion vision methodology (Fisch and Clark 2021).

The remaining two parameters are tailored for mmWave sensing and represent our innovations: (5) Velocity $v_i \in \mathbb{R}^3$

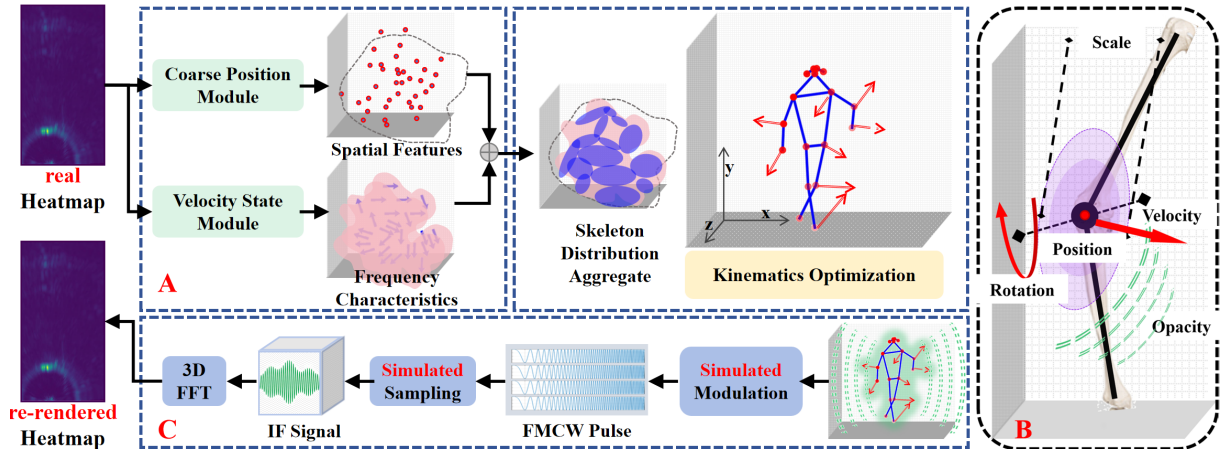


Figure 5: M-GS Processing Flow, which includes: (A) Extraction for DIPR (Sec. 5.1); (B) Association and Presentation for DIPR (Sec. 5.2); (C) Backward re-rendering for DIPR (Sec. 5.3).

captures instantaneous motion in mmWave, and (6) Doppler features $\phi_i \in \mathbb{R}^{N_d}$ encodes frequency-domain characteristics of radar reflections, where N_d represents the Doppler frequency bins. Each element $\phi_{i,k}$ corresponds to the complex amplitude at Doppler frequency bin k , capturing the spectral signature of motion-induced signal variations.

The covariance matrix Σ_i governing the Gaussian spatial distribution follows GS’s decomposition in Eq.2, but incorporates mmWave-specific parameters: $\Sigma_i = R_i S_i S_i^T R_i^T$, where R_i is derived from quaternion q_i and $S_i = \text{diag}(s_{i,x}, s_{i,y}, s_{i,z})$ contains the joint scaling factors.

As the output of M-GS, the DIPR integrates all parameters through the following unified formulation:

$$D_i(x) = \beta_i \cdot G_i(x) \cdot \exp(j\phi_i \cdot v_i \cdot (x - p_i)), \quad (6)$$

where $D_i(x)$ represents the signal disturbance of joint i .

5.3 Re-rendering Heatmap

Following the Gaussian projection principle (Eq.4), we develop a differentiable re-rendering pipeline in M-GS to transform the DIPR parameters back into the Heatmap $H_{DIPR} \in \mathbb{R}^{R \times V \times A}$. To faithfully simulate the radar sensing process, we introduce four key adaptations, each corresponding to a radar processing characteristic (Sec. 4.1):

(1) Signal modulation M_s : We explicitly model the linear chirp signals used in mmWave radar. The projection model incorporates the time-varying frequency characteristics of chirp signals, which determine the mapping from spatial Gaussian primitives to range bins. This is achieved by simulating the beat frequency response for each Gaussian. M_s is computed as:

$$M_s^{(i)} = \exp(2\pi f_0 \tau_i), \quad (7)$$

where the $\tau_i = 2\|p_i\|/c$ is the round-trip propagation time from radar to joint i . The $f_0 = 2S\|p_i\|/c$ is the constant frequency of intermediate frequency (IF) signal generated by the mixer (Iovescu and Rao 2020), with $S = B/T_c$ is the chirp slope determined by bandwidth B and chirp duration T_c , which can be configured according to specific radar

device. This enables us to capture the temporal structure of radar returns, which is essential for accurate range encoding.

(2) Doppler modulation M_d : This integrates the Doppler effect by encoding velocity-dependent phase changes for each Gaussian primitive. Specifically, the radial velocity v_r of each joint induces a frequency shift (Chen et al. 2006) $\Delta f = 2v_r/\lambda$, where λ is the radar wavelength. This shift is implemented as a phase modulation in the simulated radar return, allowing the re-rendered Heatmap to reconstruct the V dimension accurately. The differentiable design ensures gradients can propagate through the velocity states, enabling parameter optimization. M_d is expressed as:

$$M_d^{(i)} = \exp\left(2\pi \frac{2v_{r,i}}{\lambda}\right), \quad (8)$$

where $v_{r,i} = v_i \cdot (p_i/\|p_i\|)$ is the radial velocity of joint i .

(3) Antenna array phase modulation M_{ph} : To achieve angular resolution, we simulate the phase differences across multiple antenna elements for both azimuth and elevation angles. The phase offsets $\Delta\phi_{az} = 2\pi l_{az} \sin(\theta_{az})/\lambda$ and $\Delta\phi_{el} = 2\pi l_{el} \sin(\theta_{el})/\lambda$ are applied to each Gaussian’s contribution, where l_{az} and l_{el} are the antenna spacings in horizontal and vertical arrays respectively. This enables the re-rendered Heatmap to resolve both angle dimensions, faithfully reflecting the spatial distribution of radar returns as observed by a physical antenna array. M_{ph} is given by:

$$M_{ph}^{(i)} = \exp\left(\frac{2\pi l_{az} \sin(\theta_{az,i})}{\lambda}\right) \cdot \exp\left(\frac{2\pi l_{el} \sin(\theta_{el,i})}{\lambda}\right), \quad (9)$$

where $\theta_{az,i} = \arctan(p_{i,y}/p_{i,x})$ and $\theta_{el,i} = \arctan(p_{i,z}/\sqrt{p_{i,x}^2 + p_{i,y}^2})$ are azimuth and elevation angles.

(4) Two-way path loss M_{pa} : We incorporate the unique two-way propagation loss (Piersanti, Annoni, and Cassioli 2012) of mmWave, which attenuates as $1/\|p_i\|^4$ with range $\|p_i\|$. This is in contrast to the $1/\|p_i\|^2$ attenuation in optical systems. Each joint’s amplitude is modulated by this factor,

ensuring range-dependent decay. M_{pa} is computed as:

$$M_{pa}^{(i)} = \frac{1}{\|p_i\|^4}, \quad (10)$$

The full re-rendering process is expressed as:

$$H_{DIPR} = \sum_{i=1}^N M_{pa}^{(i)} \cdot M_s^{(i)} \cdot M_d^{(i)} \cdot M_{ph}^{(i)} \cdot D_i, \quad (11)$$

where D_i is the signal disturbance from Eq. 6. This provides the first fully differentiable simulation of the mmWave radar process from human kinematic primitives.

5.4 Optimization

This subsection introduces two distinct optimization losses.

Reconstruction Constraint L_{recon} measures the similarity between the H_{DIPR} and the input Heatmap H :

$$L_{recon} = L_{IoU}(H_{DIPR}, H) = 1 - \frac{|H'_{DIPR} \cap H'|}{|H'_{DIPR} \cup H'|}, \quad (12)$$

where H'_{DIPR} and H' represent masks obtained by thresholding the top $T\%$ values from H_{DIPR} and H .

Kinesiological Constraint L_{kine} operates on DIPR to ensure anatomical plausibility. To guide the position and velocity parameters exclusively, we establish two constraints: Skeletal Length Constraint, which ensures the distances between adjacent joints remain within plausible ranges, and Adjacent Joint Velocity Constraint, which ensures adjacent joints maintain consistent velocity along the bone direction.

$$L_{kine} = \lambda_1 L_{bone} + (1 - \lambda_1) L_{velocity}, \quad (13)$$

where $L_{bone} = \sum_{(i,j)} (\|p_i - p_j\| - l_{ij})^2$ enforces skeletal length constraints and $L_{velocity} = \sum_{(i,j)} \|(v_i - v_j) \cdot (p_i - p_j) / \|p_i - p_j\|\|^2$ ensures adjacent joint velocity consistency. Here p_i and v_i represent the position and velocity of joint i , λ_1 is the balancing weight, and l_{ij} are the standard bone lengths computed as mean distances between adjacent joints i and j in the dataset.

Overall loss The overall loss balances two constraints:

$$L_{total} = \lambda_2 L_{recon} + (1 - \lambda_2) L_{kine}, \quad (14)$$

where the λ_2 represent balancing weight.

6 Experiment

6.1 Experimental Setup

Implementation Environment We implement DIPR using PyTorch 2.0 with CUDA 11.8. Training is conducted on an RTX 4060 GPU with 8GB VRAM.

Dataset	Method	Input	MAJPE↓	PA-MAJPE↓
MMVR	RETR	HM(Yataka et al. 2024)	73.05	66.97
		DIPR	64.71 (↓ 8.34)	58.91 (↓ 8.06)
	HuPrModel	DIPR-HM	69.30 (↓ 3.75)	61.60 (↓ 5.37)
		HM(Lee et al. 2023)	70.24	64.88
		DIPR	60.34 (↓ 9.9)	55.07 (↓ 9.81)
		DIPR-HM	63.56 (↓ 6.68)	57.80 (↓ 7.08)
mmDiff	PC(Fan et al. 2024)	68.62	62.11	
	DIPR	61.57 (↓ 7.05)	54.99 (↓ 7.12)	
	DIPR-PC	67.90 (↓ 0.72)	59.07 (↓ 3.04)	
	PFormerV2	DIPR	62.42	56.93
HuPR	RETR	HM	78.09	72.54
		DIPR	73.74 (↓ 4.35)	67.70 (↓ 4.84)
	HuPrModel	DIPR-HM	75.90 (↓ 2.19)	70.84 (↓ 1.70)
		HM	65.37	58.11
		DIPR	62.27 (↓ 3.1)	53.64 (↓ 4.47)
		DIPR-HM	63.21 (↓ 2.16)	55.57 (↓ 2.54)
mmDiff	PC	75.54	70.02	
	DIPR	70.95 (↓ 4.59)	62.44 (↓ 7.58)	
	DIPR-PC	73.98 (↓ 1.56)	69.11 (↓ 0.91)	
	PFormerV2	DIPR	63.34	54.87
XRF55	RETR	HM	81.77	78.90
		DIPR	72.00 (↓ 9.77)	68.71 (↓ 10.19)
	HuPrModel	DIPR-HM	77.51 (↓ 4.26)	71.90 (↓ 7.0)
		HM	80.26	76.06
		DIPR	71.04 (↓ 9.22)	67.83 (↓ 8.23)
		DIPR-HM	75.72 (↓ 4.54)	69.30 (↓ 6.76)
mmDiff	PC	79.06	74.31	
	DIPR	69.75 (↓ 9.34)	67.03 (↓ 7.28)	
	DIPR-PC	70.47 (↓ 8.59)	69.17 (↓ 5.14)	
	PFormerV2	DIPR	72.07	69.15

Table 1: Experiment results across three datasets.

Dataset and Metrics We use three datasets: the MMVR dataset (Rahman et al. 2024), the HuPR dataset (Lee et al. 2023), and the XRF55 (Wang et al. 2024) dataset. Due to the lack of the Doppler dimension in MMVR’s Heatmap, we design a gradient-based velocity extraction, which estimates motion states through spatial-temporal variations across consecutive frames. In this paper, we only work on HPE tasks with single subjects. Through statistical analysis across three datasets, we establish the L_{recon} threshold T at 10%, with λ_1 at 0.5 and λ_2 at 0.3. We use the mean joint position error (MPJPE) and procrustes aligned mean joint position error (PA-MPJPE) to measure estimation accuracy.

6.2 Experiment Results

Baseline Methods We evaluate DIPR with four methods: 1) RETR (Yataka et al. 2024) is a Heatmap-based method adapted for detection in radar sensing. 2) mmDiff (Fan et al. 2024) is a PC-based method that iteratively refines pose estimates through conditional denoising. We integrate it with DIPR by generating DIPR-PC through CFAR processing on rendered Heatmap (DIPR-HM). 3) HuPrModel (Lee et al. 2023) is a Heatmap-based method utilizing multi-scale feature fusion to capture hierarchical pose features. 4) PFormerV2 (Zhao et al. 2023) is a vision method that incorporates spatio-temporal feature fusion. Compared to Heatmap’s non-3D spatial coordinate feature distribution and PC’s sparsity, DIPR’s spatio-temporal parameters align with PFormerV2’s architecture, making DIPR a suitable input paradigm. Table 1 presents results across three datasets.

Performance Comparison Table 1 presents evaluation results across four methods on three datasets. Results demonstrate DIPR’s consistent superiority over traditional

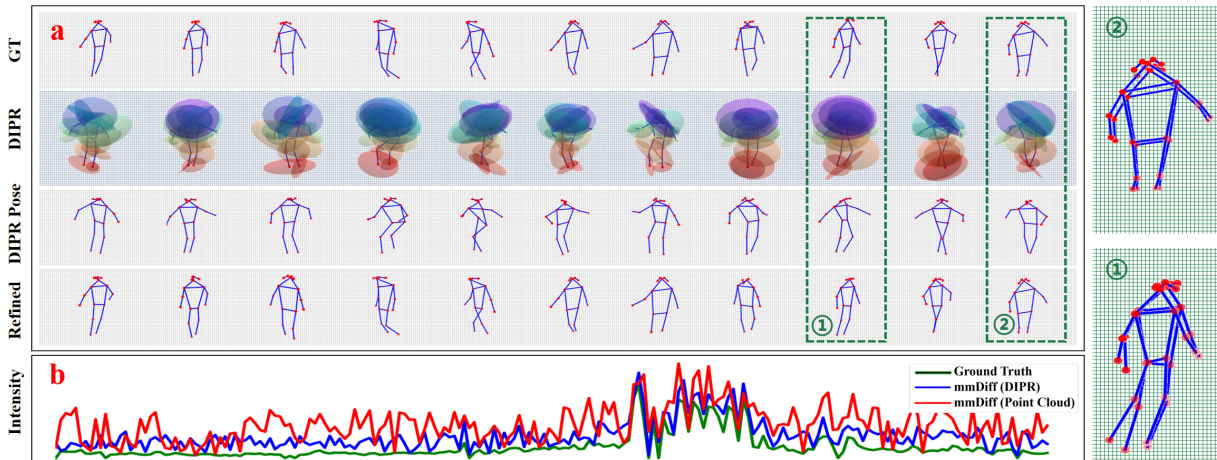


Figure 6: Visualization of DIPR: (a) Comparison of ground truth (GT), DIPR, DIPR’s pose, and mmDiff-refined DIPR’s pose. Two frames (① are zoomed, ②). (b) Inter-frame intensity of GT, mmDiff with PC (Fan et al. 2024), and mmDiff with DIPR.

paradigms: DIPR achieves significant improvements across all methods, with HuprModel reaching 60.34 MPJPE and mmDiff achieving 54.99 PA-MPJPE on the MMVR dataset. Even DIPR-HM and DIPR-PC show substantial gains compared to their original inputs, with DIPR-HM improving HuprModel by 6.68 MPJPE and DIPR-PC enhancing mmDiff by 3.04 PA-MPJPE. These improvements show DIPR’s ability to solve the limitations of traditional paradigms: DIPR’s physics-driven formulation effectively mitigates Heatmap’s high noise disturbance through structured kinematic constraints, while its continuous 3D representation resolves PC’s sparsity by providing dense, temporally coherent features. PFormerV2, originally designed for vision-based pose estimation, demonstrates competitive performance when adapted with DIPR, validating the DIPR’s capability to bridge vision-based HPE with mmWave sensing through unified spatio-temporal modeling.

Visualization Fig. 6 (a) illustrates evolution with mmDiff (Fan et al. 2024), which is selected as the baseline due to its explicit focus on temporal consistency through conditional denoising diffusion. In DIPR, each distribution is depicted as an ellipsoid that encodes the instantaneous motion state. Notably, DIPR itself exhibits high accuracy in pose estimation. The subsequent mmDiff refinement further enhances the alignment. Following (Fan et al. 2024), we use inter-frame motion intensity (Fig. 6 (b)) to measure temporal consistency, where better consistency is indicated by intensity curves that more closely match the ground truth pattern. The result demonstrates that DIPR-based mmDiff exhibits superior temporal consistency compared to original PC-based mmDiff, with intensity curves that follow the ground truth more faithfully and show significantly reduced erratic fluctuations. This validates DIPR’s capability to provide more stable motion features compared with PC.

Ablation on Position and Velocity Modules To better understand the contribution of extraction modules in M-GS, we conduct ablation studies on the Coarse Position module (P)

Model	M-GS	Input	MMVR MAJPE↓	HuPR MAJPE↓	XRF55 MAJPE↓
RETR	P	DIPR-HM	89.74 (↑20.44)	84.05 (↑8.15)	89.43 (↑11.92)
RETR	V	DIPR-HM	71.92 (↑2.62)	78.11 (↑2.21)	80.45 (↑2.94)
RETR	P+V	DIPR-HM	69.30	75.90	77.51
mmDiff	P	DIPR-PC	85.03 (↑16.32)	81.39 (↑7.41)	87.71 (↑17.24)
mmDiff	V	DIPR-PC	68.71 (↑0.81)	74.60 (↑0.62)	76.42 (↑5.95)
mmDiff	P+V	DIPR-PC	67.90	73.98	70.47

Table 2: Ablation on position and velocity modules.

M_s	M_d	M_{ph}	M_{pa}	MAJPE↓	PA-MAJPE↓
✓	✓	✓	✓	64.71	58.91
×	✓	✓	✓	90.30	84.17
✓	×	✓	✓	89.00	82.66
✓	✓	×	✓	70.92	65.05
✓	✓	✓	×	66.84	60.27

Table 3: Ablation of four modules in re-rendering (Eq. 11).

and Velocity State modules (V) by replacing their outputs with zero tensors, as both are required for re-rendering. We observe that (Table 2) removing the V leads to a significant error increase due to unremoved non-human noise, while removing the P causes a milder decline, as velocity information still provides useful spatial cues for joint localization.

Ablation on Re-render Adaptation Modules We also study the effectiveness of four re-rendering modules (Eq. 11) in Sec. 5.3. Table 3 presents the results using RETR on the MMVR dataset. Removing either the M_s (Eq. 7) or the M_d (Eq. 8) leads to a substantial performance degradation, indicating that accurate range encoding and velocity modulation are critical. Excluding the M_{ph} (Eq. 9) also degrades performance, highlighting the importance of angular resolution. Omitting the M_{pa} (Eq. 10) results in a moderate performance drop, suggesting that realistic amplitude attenuation contributes to, but is less dominant in, overall accuracy.

Additional Results To better understand DIPR’s robustness and complexity, we conduct ablations on constraint weights λ_1 and λ_2 , reconstruction thresholds T , and perform

computational efficiency analysis. We also visualize comparisons on the ground truth's pose, DIPR's pose, along with comparisons on DIPR-HM and DIPR-PC with real Heatmap and PC. Results are provided in the Supplementary.

7 Conclusion

To address the limitations of Heatmap's high noise distribution and PC's sparsity issues in mmWave-based HPE, we propose DIPR, a differentiable physics-driven human representation paradigm along with its synthesis method M-GS. By synthesizing human biomechanical principles with mmWave propagation physics, DIPR attenuates the ambiguity and stochasticity inherent in network-driven methods. Experiments across three datasets with four approaches demonstrate DIPR's consistent superiority over Heatmap and PC. The integration of DIPR yields significant performance boosts across all evaluated methods, establishing new state-of-the-art results on all datasets. However, the current DIPR is designed for single-subject scenarios and may face challenges in multi-person environments due to overlap and occlusion, which present directions for future research.

References

- Abdal, R.; Yifan, W.; Shi, Z.; Xu, Y.; Po, R.; Kuang, Z.; Chen, Q.; Yeung, D.-Y.; and Wetzstein, G. 2024. Gaussian shell maps for efficient 3d human generation. In *Proceedings of the IEEE/CVF Conference on Computer Vision and Pattern Recognition*, 9441–9451.
- An, S.; Li, Y.; and Ogras, U. 2022. mri: Multi-modal 3d human pose estimation dataset using mmwave, rgb-d, and inertial sensors. *Advances in neural information processing systems*, 35: 27414–27426.
- An, S.; and Ogras, U. Y. 2022. Fast and scalable human pose estimation using mmwave point cloud. In *Proceedings of the 59th ACM/IEEE Design Automation Conference*, 889–894.
- Bao, Y.; Zhao, X.; and Qian, D. 2024. Hybrid 3D Human Pose Estimation with Monocular Video and Sparse IMUs. *arXiv preprint arXiv:2404.17837*.
- Bi, Z.; Gao, Y.; Wang, C.; Liu, Z.; Wan, Y.; and Yang, X. 2023. Recursive spatial-temporal clustering-based target detection with millimeter-wave radar point cloud. *Measurement Science and Technology*, 34(7): 075110.
- Cao, Z.; Ding, W.; Chen, R.; Zhang, J.; Guo, X.; and Wang, G. 2022. A joint global–local network for human pose estimation with millimeter wave radar. *IEEE Internet of Things Journal*, 10(1): 434–446.
- Chang, S.; Zhang, Y.; Zhang, F.; Zhao, X.; Huang, S.; Feng, Z.; and Wei, Z. 2020. Spatial attention fusion for obstacle detection using mmwave radar and vision sensor. *Sensors*, 20(4): 956.
- Chen, V. C.; Li, F.; Ho, S.-S.; and Wechsler, H. 2006. Micro-Doppler effect in radar: phenomenon, model, and simulation study. *IEEE Transactions on Aerospace and electronic systems*, 42(1): 2–21.
- Ding, F.; Luo, Z.; Zhao, P.; and Lu, C. X. 2024. milliflow: Scene flow estimation on mmwave radar point cloud for human motion sensing. In *European Conference on Computer Vision*, 202–221. Springer.
- Fan, J.; Yang, J.; Xu, Y.; and Xie, L. 2024. Diffusion model is a good pose estimator from 3d rf-vision. In *European Conference on Computer Vision*, 1–18. Springer.
- Fisch, M.; and Clark, R. 2021. Orientation keypoints for 6D human pose estimation. *IEEE Transactions on Pattern Analysis and Machine Intelligence*, 44(12): 10145–10158.
- Gurbuz, S. Z.; and Amin, M. G. 2019. Radar-based human-motion recognition with deep learning: Promising applications for indoor monitoring. *IEEE Signal Processing Magazine*, 36(4): 16–28.
- He, K.; Zhang, X.; Ren, S.; and Sun, J. 2016. Deep residual learning for image recognition. In *Proceedings of the IEEE conference on computer vision and pattern recognition*, 770–778.
- Ho, J.; Jain, A.; and Abbeel, P. 2020. Denoising diffusion probabilistic models. *Advances in neural information processing systems*, 33: 6840–6851.
- Iovescu, C.; and Rao, S. 2020. The fundamentals of millimeter wave radar sensors. *Texas Instruments*, 1–7.
- Jayaweera, S. S.; Regani, S. D.; Hu, Y.; Wang, B.; and Liu, K. R. 2024. HRNet: High-Resolution Neural Network for Human Imaging Using mmWave Radar. *IEEE Internet of Things Journal*.
- Kocabas, M.; Chang, J.-H. R.; Gabriel, J.; Tuzel, O.; and Ranjan, A. 2024. Hugs: Human gaussian splats. In *Proceedings of the IEEE/CVF conference on computer vision and pattern recognition*, 505–515.
- Lee, S.-P.; Kini, N. P.; Peng, W.-H.; Ma, C.-W.; and Hwang, J.-N. 2023. Hupr: A benchmark for human pose estimation using millimeter wave radar. In *Proceedings of the IEEE/CVF Winter Conference on Applications of Computer Vision*, 5715–5724.
- Li, Z.; Zheng, Z.; Wang, L.; and Liu, Y. 2024. Animatable gaussians: Learning pose-dependent gaussian maps for high-fidelity human avatar modeling. In *Proceedings of the IEEE/CVF conference on computer vision and pattern recognition*, 19711–19722.
- Loper, M.; Mahmood, N.; Romero, J.; Pons-Moll, G.; and Black, M. J. 2023. SMPL: A skinned multi-person linear model. In *Seminal Graphics Papers: Pushing the Boundaries, Volume 2*, 851–866.
- Luiten, J.; Kopanas, G.; Leibe, B.; and Ramanan, D. 2024. Dynamic 3d gaussians: Tracking by persistent dynamic view synthesis. In *2024 International Conference on 3D Vision (3DV)*, 800–809. IEEE.
- Nibali, A.; He, Z.; Morgan, S.; and Prendergast, L. 2019. 3d human pose estimation with 2d marginal heatmaps. In *2019 IEEE Winter Conference on Applications of Computer Vision (WACV)*, 1477–1485. IEEE.
- Niu, Y.; Li, Y.; Jin, D.; Su, L.; and Vasilakos, A. V. 2015. A survey of millimeter wave communications (mmWave) for 5G: opportunities and challenges. *Wireless networks*, 21: 2657–2676.

Piersanti, S.; Annoni, L. A.; and Cassioli, D. 2012. Millimeter waves channel measurements and path loss models. In *2012 IEEE International Conference on Communications (ICC)*, 4552–4556. IEEE.

Rahman, M. M.; Yataka, R.; Kato, S.; Wang, P.; Li, P.; Cardace, A.; and Boufounos, P. 2024. MMVR: Millimeter-Wave Multi-view Radar Dataset and Benchmark for Indoor Perception. In *European Conference on Computer Vision*, 306–322. Springer.

Rohling, H. 1983. Radar CFAR thresholding in clutter and multiple target situations. *IEEE transactions on aerospace and electronic systems*, (4): 608–621.

Sengupta, A.; and Cao, S. 2022. mmpose-nlp: A natural language processing approach to precise skeletal pose estimation using mmwave radars. *IEEE Transactions on Neural Networks and Learning Systems*, 34(11): 8418–8429.

Sengupta, A.; Jin, F.; Zhang, R.; and Cao, S. 2020. mm-Pose: Real-time human skeletal posture estimation using mmWave radars and CNNs. *IEEE Sensors Journal*, 20(17): 10032–10044.

Singh, A. D.; Sandha, S. S.; Garcia, L.; and Srivastava, M. 2019. Radhar: Human activity recognition from point clouds generated through a millimeter-wave radar. In *Proceedings of the 3rd ACM Workshop on Millimeter-wave Networks and Sensing Systems*, 51–56.

Wang, F.; Lv, Y.; Zhu, M.; Ding, H.; and Han, J. 2024. Xrf55: A radio frequency dataset for human indoor action analysis. *Proceedings of the ACM on Interactive, Mobile, Wearable and Ubiquitous Technologies*, 8(1): 1–34.

Wang, Z.; Jiang, D.; Sun, B.; and Wang, Y. 2023. A data augmentation method for human activity recognition based on mmwave radar point cloud. *IEEE Sensors Letters*, 7(5): 1–4.

Wu, G.; Yi, T.; Fang, J.; Xie, L.; Zhang, X.; Wei, W.; Liu, W.; Tian, Q.; and Wang, X. 2024. 4D Gaussian Splatting for Real-Time Dynamic Scene Rendering. In *Proceedings of the IEEE/CVF Conference on Computer Vision and Pattern Recognition (CVPR)*, 20310–20320.

Xue, H.; Cao, Q.; Miao, C.; Ju, Y.; Hu, H.; Zhang, A.; and Su, L. 2023. Towards generalized mmwave-based human pose estimation through signal augmentation. In *Proceedings of the 29th Annual International Conference on Mobile Computing and Networking*, 1–15.

Yataka, R.; Cardace, A.; Wang, P.; Boufounos, P.; and Takahashi, R. 2024. RETR: Multi-view radar detection transformer for indoor perception. *Advances in Neural Information Processing Systems*, 37: 19839–19869.

Zhang, D.; Zhang, X.; Xie, Y.; Zhang, F.; Yang, H.; and Zhang, D. 2024. From single-point to multi-point reflection modeling: Robust vital signs monitoring via mmwave sensing. *IEEE Transactions on Mobile Computing*.

Zhang, G.; Geng, X.; and Lin, Y.-J. 2021. Comprehensive mpoint: A method for 3d point cloud generation of human bodies utilizing fmcw mimo mm-wave radar. *Sensors*, 21(19): 6455.

Zhao, M.; Li, T.; Abu Alsheikh, M.; Tian, Y.; Zhao, H.; Torralba, A.; and Katabi, D. 2018a. Through-wall human pose estimation using radio signals. In *Proceedings of the IEEE conference on computer vision and pattern recognition*, 7356–7365.

Zhao, M.; Tian, Y.; Zhao, H.; Alsheikh, M. A.; Li, T.; Hristov, R.; Kabelac, Z.; Katabi, D.; and Torralba, A. 2018b. RF-based 3D skeletons. In *Proceedings of the 2018 Conference of the ACM Special Interest Group on Data Communication*, 267–281.

Zhao, Q.; Zheng, C.; Liu, M.; Wang, P.; and Chen, C. 2023. Poseformerv2: Exploring frequency domain for efficient and robust 3d human pose estimation. In *Proceedings of the IEEE/CVF conference on computer vision and pattern recognition*, 8877–8886.

Zhu, B.; He, Z.; Xiong, W.; Ding, G.; Liu, J.; Huang, T.; Chen, W.; and Xiang, W. 2024. ProbRadarM3F: mmWave Radar based Human Skeletal Pose Estimation with Probability Map Guided Multi-Format Feature Fusion. *arXiv preprint arXiv:2405.05164*.

A Additional Quantitative Results

A.1 Ablation Study on Kinematic Constraints

To investigate how kinematic constraints enhance DIPR’s ability to filter out non-human noise while preserving motion features, we conduct ablation studies on the skeletal length constraint and adjacent joint velocity constraint (Eq.13) using RETR as the baseline model. RETR (Yataka et al. 204) is selected for its Heatmap-centric architecture that naturally aligns with DIPR’s physics-driven approach. Table 1 presents performance comparisons across different weight combinations.

Results demonstrate that equal weighting ($\lambda_1 = 0.5$) achieves optimal performance, balancing anatomical plausibility with motion flexibility. The velocity constraint shows higher sensitivity to weight variations, indicating that consistent motion patterns between adjacent joints are crucial for mitigating Heatmap noise through temporal coherence. Performance degradation when constraints are removed validates DIPR’s capability to provide structured kinematic information that guides joint localization.

Length ; Velocity	HuPR	HuPR	MMVR	MMVR	XRF55	XRF55
	MAJPE↓	PAMAJPE↓	MAJPE↓	PAMAJPE↓	MAJPE↓	PAMAJPE↓
0.0:1.0	80.04	75.72	74.08	73.59	78.45	76.00
0.3: 0.7	76.37	72.56	72.57	69.83	77.09	74.51
0.5:0.5	73.74	67.70	71.08	65.17	72.00	68.71
0.3:0.7	76.54	73.19	73.87	70.03	77.16	74.19
1.0:0.0	81.69	77.43	74.19	73.80	80.59	77.51

Table 4: Ablation on λ_1 (Eq. 13) of Skeletal Length Constraint and Adjacent Joint Velocity Constraint with RETR.

A.2 Ablation Study on Reconstruction Threshold

To investigate the impact of different intensity thresholds T in the reconstruction constraint (Eq. 12) on overall performance. Table 2 shows results obtained by varying the top T value from 5% to 100%.

The experimental findings reveal that a 10% threshold provides the optimal balance between signal preservation and noise suppression. Higher top T (30%-100%) retain excessive noise from the original Heatmap, leading to performance degradation, while lower top T (5%) discard valuable human motion information. This selection is consistent across all three datasets, demonstrating DIPR’s effectiveness in mitigating Heatmap noise while preserving essential motion features through its physics-driven formulation.

T	HuPR		MMVR		XRF55	
	MAJPE↓	PAMAJPE↓	MAJPE↓	PAMAJPE↓	MAJPE↓	PAMAJPE↓
5%	75.01	71.43	76.82	70.45	75.96	72.65
10%	73.74	67.70	71.08	65.17	72.00	68.71
30%	87.13	81.61	80.08	74.86	77.14	73.40
70%	88.03	81.95	80.09	74.90	77.11	73.67
100%	88.17	82.05	80.51	75.47	77.89	75.03

Table 5: Ablation on Heatmap mask threshold in reconstruction constraint with RETR.

A.3 Ablation Study on Constraint Balancing

To understand how DIPR balances noise suppression with motion preservation (Eq. 14), we conduct experiments with different weight λ_2 combinations. Table 3 presents results obtained by varying the ratio between reconstruction and kinematic constraint weights.

Experimental results demonstrate dataset-dependent optimal weightings: MMVR dataset achieves best performance with equal weighting (0.5:0.5), while HuPR and XRF55 datasets prefer reconstruction constraint (0.3:0.7). This variation suggests that some datasets (HuPR, XRF55) might have higher noise levels, and DIPR benefits more from reconstruction constraint’s noise suppression, while other datasets with complex motion patterns require stronger kinematic guidance. This analysis validates DIPR’s adaptive capability to address both Heatmap noise and PC sparsity based on dataset characteristics.

Recon: Kines	HuPR		MMVR		XRF55	
	MAJPE↓	PAMAJPE↓	MAJPE↓	PAMAJPE↓	MAJPE↓	PAMAJPE↓
0.0:1.0	90.30	84.17	80.51	75.47	78.09	75.72
0.3:0.7	73.74	67.70	71.08	65.17	72.00	68.71
0.5:0.5	74.84	70.03	64.71	58.91	74.64	70.50
0.7:0.3	75.31	72.47	75.08	72.33	77.09	74.63
1.0:0.0	80.88	75.93	78.73	74.11	78.09	75.72

Table 6: Ablation on λ_2 (Eq. 14) of reconstruction and kinematic constraint with RETR.

A.4 Model Computational Cost Analysis

To demonstrate how DIPR’s physics-driven formulation addresses computational efficiency while solving noise and sparsity issues, we conduct a analysis on model complexity and computational cost trade-offs. We conduct experiments on the MMVR dataset (Rahman et al. 2024) using mmDiff (Fan et al. 2024) embedded with a RetNet (He et al. 2016) pre-trained module. The mmDiff originally used PC as the input paradigm. We used a simple MLP network as shown in Fig. 1 for comparative experiments.

Method	Input	Size	Inference	Memory	MAJPE ↓	PA-MAJPE ↓
mmDiff	PC	362.8M	24ms	8.0 G	68.62	62.11
MLP	DIPR	3.9M	4ms	0.5 G	72.50	69.11
mmDiff	DIPR	91.2M	18ms	3.6 G	61.57	54.99

Table 7: Performance and computational cost comparison between PC-based mmDiff (Fan et al. 2024), DIPR-based MLP, and DIPR-based mmDiff

Table 4 compares the performance and computational costs of different configurations. The results demonstrate DIPR’s significant efficiency advantages: the MLP-based approach with DIPR input achieves comparable performance to the full mmDiff model while requiring only 1.1% of the parameters, 16% of the inference time, and 6.25% of the memory usage. This efficiency improvement directly addresses the computational overhead associated with processing the noisy Heatmap. When DIPR is integrated with the full mmDiff, we observe substantial performance improvements across all evaluation metrics while maintaining reasonable computational overhead, demonstrating that DIPR’s rich representation enhances the model’s capability without significantly increasing computational complexity.

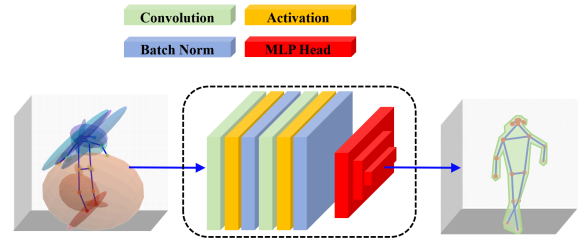


Figure 7: Architecture of the lightweight MLP model, which consists of fully connected layers that process the parameterized DIPR.

B Additional Visualization Results

B.1 Qualitative Comparison: Ground Truth vs. DIPR Skeleton

To demonstrate the effectiveness of DIPR in accurately capturing human pose from mmWave signals, we present comparisons between ground truth skeletons and our DIPR-estimated skeletons across various motion sequences (Fig. 8, 9). These visualizations showcase DIPR’s capability to reconstruct human poses with high fidelity while maintaining anatomical plausibility.

B.2 Comparison of Heatmap and Point Cloud Representations

To demonstrate how DIPR addresses the limitations of Heatmap noise and PC sparsity in human pose estimation, we present qualitative comparisons of the original and DIPR-generated Heatmap and PC (Fig. 4,5).

The results demonstrate that DIPR effectively addresses noise and sparsity issues in traditional paradigms. Specifically, the DIPR-Heatmap exhibits significantly cleaner pat-

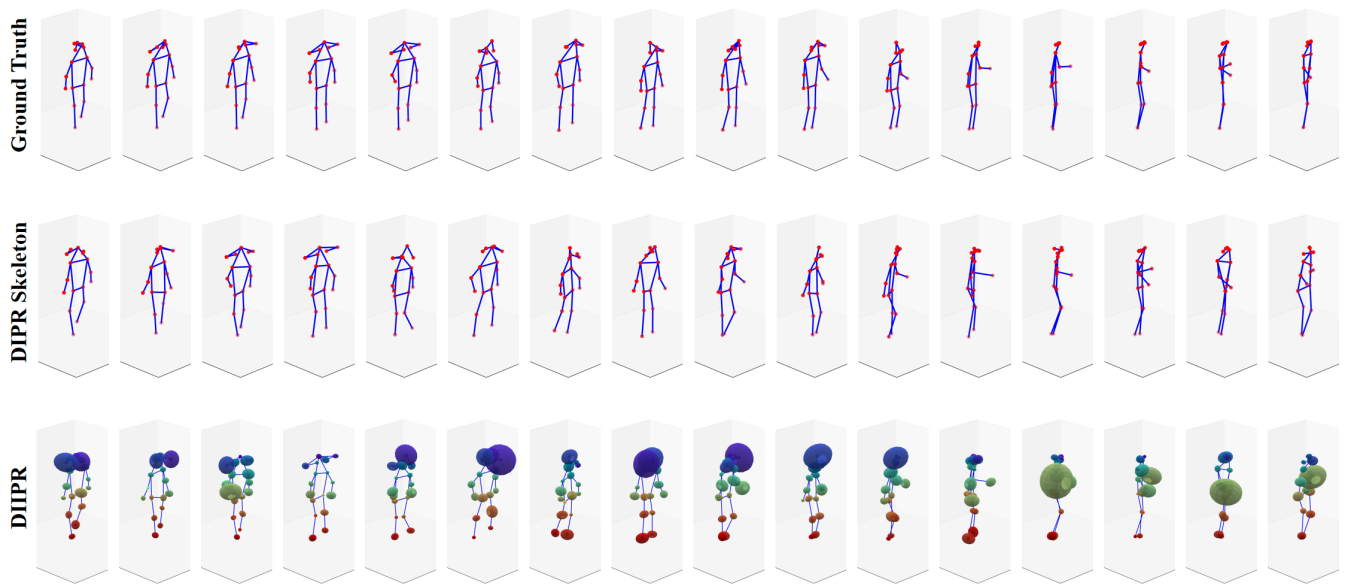


Figure 8: Ground Truth Skeleton, Skeleton in DIPR, Skeleton and Velocity in DIPR

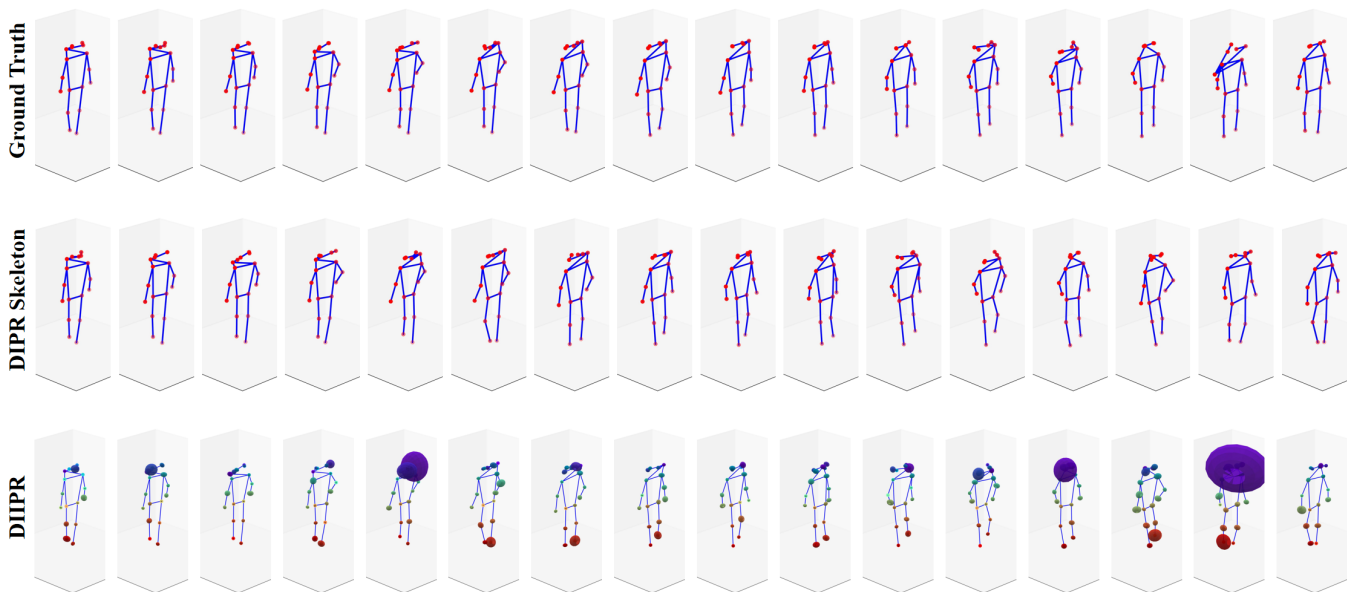


Figure 9: Ground Truth Skeleton, Skeleton in DIPR, Skeleton and Velocity in DIPR

terns with reduced background noise and more coherent signal distributions compared to the original Heatmap, effectively mitigating the high noise distribution problem. Similarly, the DIPR-PC is substantially denser and more structured, forming more recognizable human-like shapes that overcome the severe sparsity of traditional Point Clouds. This enhancement in signal quality ensures that DIPR better preserves crucial human motion characteristics, providing a richer and more informative input for downstream pose estimation tasks.

B.3 Re-rendering Effect with Different Heatmap Thresholds

To understand how DIPR effectively mitigates the inherent noise of raw Heatmap and reconstructs meaningful pose information, we investigate the impact of varying reconstruction constraint thresholds top T (Eq. 12) on the quality of the re-rendered Heatmap (Fig. 6).

The visualization demonstrates that threshold selection significantly affects the trade-off between noise suppression and feature preservation. Lower top T , such as 5%, results in highly sparse and fragmented patterns, effectively suppressing noise but at the cost of losing crucial pose-related features. As the T increases to 10%, the re-rendered Heatmap exhibits cleaner and more coherent patterns, indicating effective noise reduction while retaining sufficient structural details. Conversely, higher T (e.g., 70%, 100%) progressively recover more fine-grained details but simultaneously reintroduce significant noise, making the re-rendered Heatmap increasingly resemble the noisy original input. This highlights the critical balance required. The top 10% threshold provides the optimal balance, effectively addressing the noise inherent in raw Heatmap while preserving the essential kinematic features, as further confirmed by our quantitative results in Table 2. This analysis underscores DIPR’s capability to generate cleaner, more informative representations for robust mmWave-based HPE.

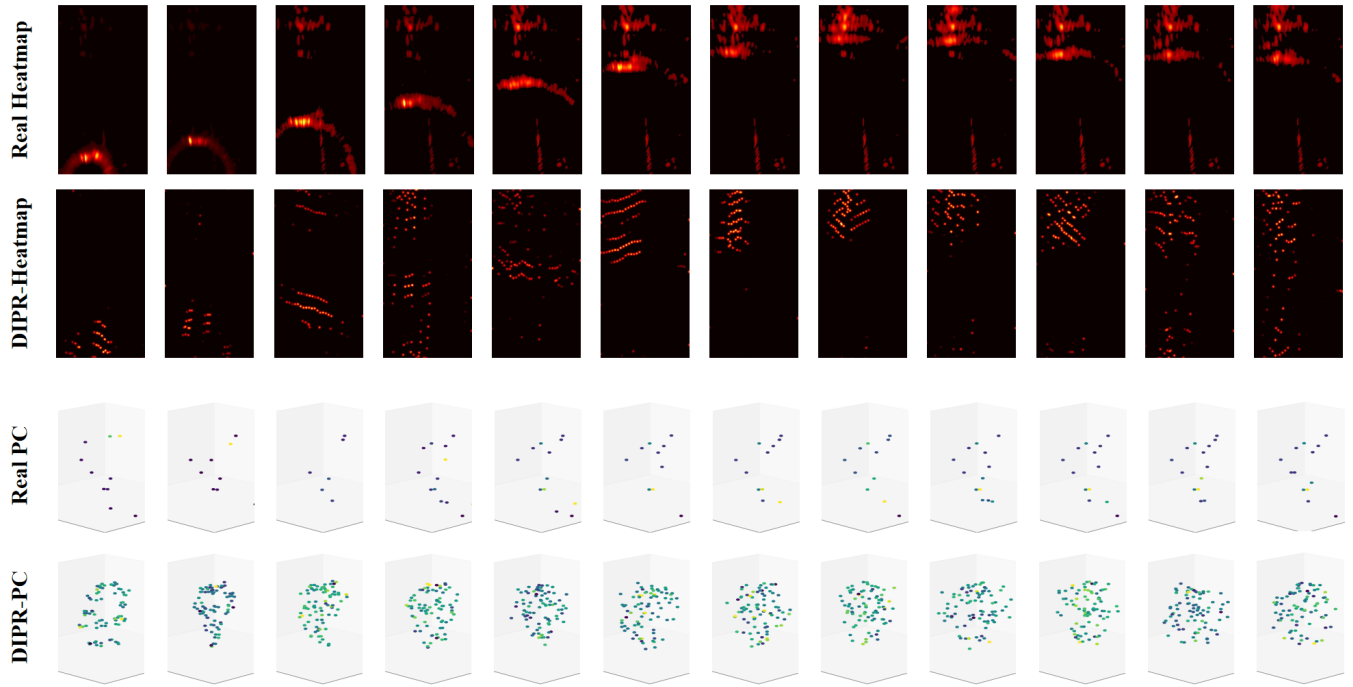


Figure 10: Original Heatmap, DIPR-Heatmap, Real Point Cloud, DIPR-Point Cloud

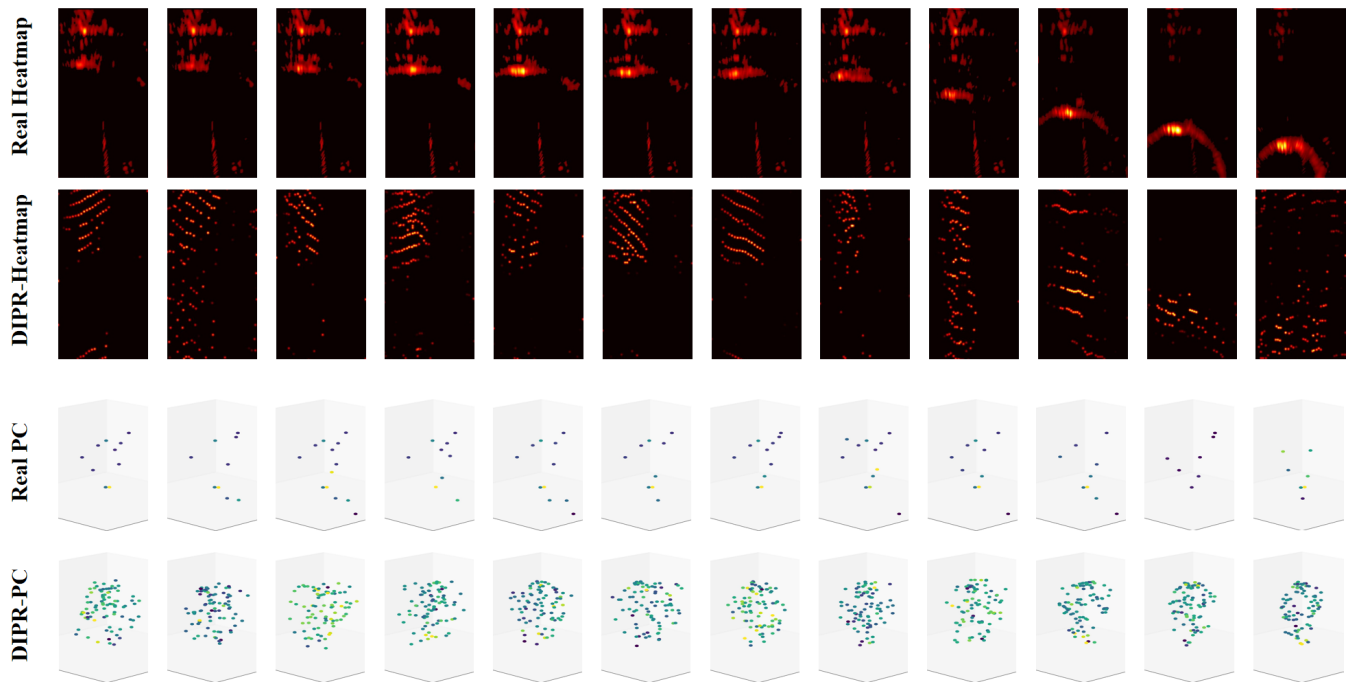


Figure 11: Original Heatmap, DIPR-Heatmap, Real Point Cloud, DIPR-Point Cloud

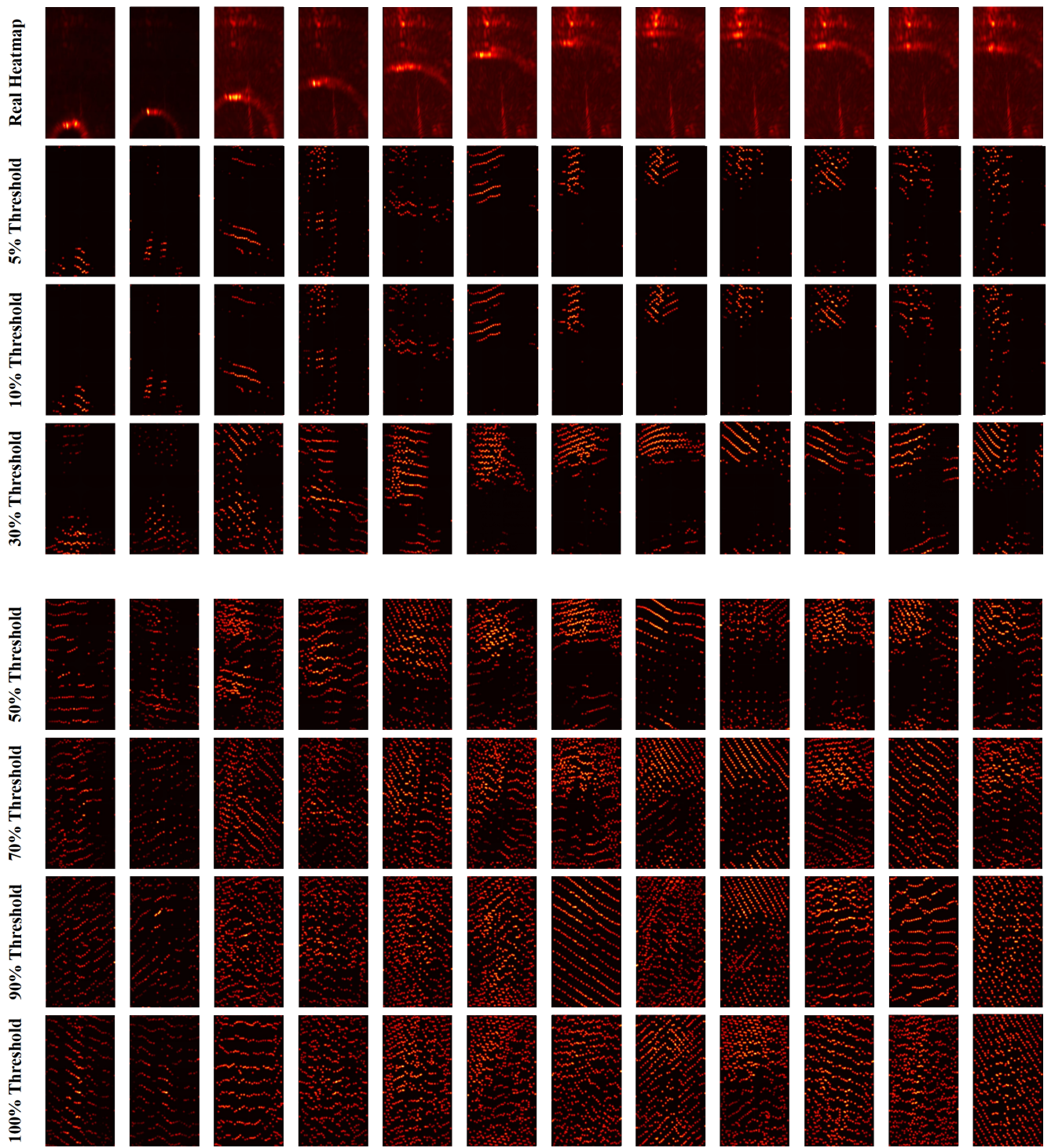


Figure 12: Original Heatmap and Re-rendered Heatmap under different thresholds in reconstruction constraint